Corrosion Science 218 (2023) 111162

Contents lists available at ScienceDirect

Corrosion Science

journal homepage: www.elsevier.com/locate/corsci

The structure dependence of oxidation behavior of high-angle grain boundaries of alloy 600 in simulated pressurized water reactor primary water

Xingyu Feng [1], Qi Wang [1], Jiayu Xie, Wenjun Kuang [*]

Center for Advancing Materials Performance from the Nanoscale (CAMP-Nano), State Key Laboratory for Mechanical Behavior of Materials, Xi'an Jiaotong University, Xi'an 710049, PR China

ARTICLE INFO

Keywords:
Alloy 600
STEM
Grain boundary diffusion
Grain boundary migration
Intergranular oxidation

ABSTRACT

The intergranular degradation of seven different types of high-angle grain boundaries (HAGBs) were investigated on Alloy 600 after exposure to simulated pressurized water reactor primary water. All boundaries are susceptible to preferential intergranular oxidation (PIO) except for ideal coherent twin boundary. Diffusion induced grain boundary migration (DIGM) normally occurs and its depth is positively correlated with the PIO extent. Interestingly, the PIO susceptibility is independent on the grain boundary misorientation angle or Σ value, but related to the grain boundary atom packing density (GBAPD). Grain boundaries with higher GBAPD values show higher PIO resistance as the element diffusion is slower.

1. Introduction

Nickel base Alloy 600 was widely used in pressurized water reactors (PWRs) owing to its high corrosion resistance and good mechanical properties [1]. However, stress corrosion cracking (SCC) has been frequently reported in Alloy 600 under both PWR service and laboratory test conditions [2–5]. Several models have been proposed to explain the intergranular stress corrosion cracking (IGSCC) phenomenon. Among them, selective internal oxidation mechanism appears to be the most comprehensive one and is gaining increasing acceptance [6–9]. The model was further improved by Bertali et al. [10] and adapted to preferential intergranular oxidation (PIO) model. Under high temperature water or steam condition, O ingress occurs along the grain boundaries (GBs) and forms oxides with the less noble metals. Meanwhile, Cr and Fe diffuse outwards and induce grain boundary migration. The bonding strength of GB is significantly decreased and the oxidized boundary tends to crack under stress [9,11–14]. So PIO is an indispensable precursor event for IGSCC initiation. Kanzaki et al. [15] also found that the SCC susceptibility of Ni-Cr-Fe alloys under simulated PWR primary condition is closely related to the GB oxidation depth. Now increasing researches indicate that this PIO model also applies to the SCC of stainless steel [16–21] as well as irradiation assisted SCC [22–25].

It is well known that grain boundary structure plays an important role in intergranular oxidation behavior [26–30]. Based on the coincidence site lattice (CSL) model, GBs can be classified into three types, low-angle grain boundaries (LAGBs, namely Σ1), low-Σ ($3 \leq \Sigma \leq 29$) CSL and random high-angle grain boundaries (RHABs). The low-angle and low-Σ GBs are generally regarded as 'special' ones due to their high resistance to intergranular degradation [1,31–34]. For instance, Lim et al. [30] found that Σ3 twin boundary of Alloy 600 is immune to oxidation and Σ9 boundary possess a higher oxidation resistance than RHAB after immersion test in simulated PWR primary water. More studies on other Ni-Cr-Fe alloys also suggest that twin boundaries have significantly higher resistance to intergranular oxidation than RHAB [28,35,36]. However, except coherent twin boundary (CTB), the other 'special' GBs are still susceptible to penetrative oxidation. It has been reported that the LAGB of Alloy 600 can be oxidized in 340 ℃ primary water environment [37]. We have systematically studied the PIO behavior of LAGBs and found that all of them are susceptible to PIO, even when the misorientation angle is as low as 5.7° [38]. The Σ1 and Σ3 GBs have earned much attention due to their high proportion and distinguished structure, while very few studies have been focused on other low-Σ CSL GBs. A better understanding of the effect of GB structure on PIO behavior is necessary for predicting the IGSCC performance and improving the IGSCC resistance by grain boundary engineering treatment.

* Corresponding author.
E-mail address: wjkuang66@gmail.com (W. Kuang).
[1] These authors contributed equally to this work.

https://doi.org/10.1016/j.corsci.2023.111162
Received 28 September 2022; Received in revised form 2 March 2023; Accepted 3 April 2023
Available online 5 April 2023

The crystallographic structure of GBs can be fully determined by five degrees of freedom. Three of them describe the misorientation between the two grain matrixes, and the other two are used to determine the GB plane normal. However, CSL model only considers the misorientation angles between two adjacent grains, while the GB plane normal is not considered. As such, the CSL GBs were found to be not special in the intergranular cracking [1,34]. Therefore, the structure-performance correlation should be explored beyond the CSL concept. Now increasing results show that the GB plane play an important role in solute diffusivity and oxidation kinetics. For instance, Kuang et al. [26,27] studied the intergranular degradation behavior of Alloy 690 (which contains twice the chromium content of Alloy 600) and found that the Cr diffusivity decreases in the order of RHABs, ITBs (incoherent twin boundaries) and CTBs. They also reported that Σ3 twin boundaries (include CTB, ITB and TTB (transformed twin boundary)) of Alloy 690 show different oxidation susceptibilities even when they have a similar misorientation. The results indicate that the Cr diffusivity is related to the GB plane coherency. Minkwitz et al. [39] found the GB plane has a significant influence on GB diffusion along twin boundaries in copper. The GB diffusion coefficient increases with the GB plane deviating from {111} close-packed plane. Furthermore, An et al. [40] reported that the elemental diffusivity along high angle grain boundaries (HAGBs) depends on the atom packing density (APD) of GB plane rather than the misorientation angle in 304L stainless steel. Boundaries with higher APD shows lower degree of intergranular degradation. More recently, we also found that the APD of GB has a strong effect on solute diffusivity and susceptibility to PIO of LAGB in Alloy 600 [38]. However, the key structure parameters affecting the solute diffusivity and oxidation kinetics are still unclear in HAGBs, especially low-Σ CSL GBs (e.g. Σ5, Σ7, Σ9 and Σ11).

In this paper, we studied the influence of GB structure on the solute diffusivity and PIO susceptibility of HAGBs (including Σ3, Σ5, Σ7, Σ9, Σ11 and RHAB) in Alloy 600 after exposure to simulated PWR primary water. The full GB structure parameters (misorientation and GB plane orientation) were characterized. Subsequently, the microstructure and elemental composition of intergranular oxides and the extent of Cr diffusion were examined. The aim of this study was to understand: 1) the relationship between PIO and solute diffusivity in HAGBs, 2) the key structure parameters that dominate solute diffusion and oxidation kinetics.

2. Experimental

2.1. Material

The chemical composition of used Alloy 600 is 75.1 % Ni, 15.6 % Cr, 7.92 % Fe, 0.46 % Mn, 0.03 % Mo, 0.011 % Co, 0.22 % Si, 0.0023 % B, 0.002 % S, 0.0092 % P and 0.01 % C (in wt.%). The as-received sample block was solution annealed at 1100 ℃ for 1 h and then quenched in water. After that, square coupons with the dimensions of 10 mm × 10 mm × 2 mm were cut from the block. The sample surface was progressively ground to 4000 grit and then electropolished for 30 s at 30 V in 10 % (volume fraction) perchloric acid in methanol at − 30 ℃ to obtain a strain-free surface. Finally, the specimen was cleaned immediately with methanol and acetone.

2.2. Apparatus and methodology

Prior to exposure in the autoclave, the grain boundary structure was recorded by electron backscatter diffraction (EBSD) system in a TESCAN MIRA3 FEG scanning electron microscope (SEM). EBSD test was performed at 20 kV and 5.5 nA with a step size of 4 μm. The crystallographic data was analyzed using TSL OIM software. Here, the Brandon criterion was applied to define the CSL GB types. The grain boundary distribution and their length fractions are shown in Fig. 1.

Oxidation tests were conducted in 19 MPa, 350 ℃ water which contains 19.7 cm^3 (STP) H_2/kg H_2O (amounts to 1.8 ppm which is near the Ni/NiO boundary) in a refreshed stainless steel autoclave. 2 ppm Li was added into the water as LiOH and 1000 ppm B was added as boric acid. After exposure for 1270 h, the oxidized specimens were taken out for further characterization.

Seven different types of HAGBs, including Σ3 (coherent and incoherent twin boundaries), Σ5, Σ7, Σ9, Σ11 and RHAB, were sampled and investigated in this work. Cross section lamellas of twelve HAGBs (belongs to seven different types) were prepared using focus ion beam (FIB) milling on a FEI Helios Nanolab 600. The lamella were lift out, and gradually milled to ~ 90 nm thick with a final beam current of 47 pA at 5 kV. The oxide structure was analyzed with a JEOL JEM-2100F transmission electron microscope (TEM). Element distribution was analyzed with a Thermo-Fisher Talos F200X scanning transmission electron microscope (STEM) which is equipped with a high angle annular dark-field (HAADF) detector and a "Super X" X-ray energy dispersive spectroscopy (EDS) system consisting of four Silicon Drift Detectors. EDS mappings were acquired at 512 × 512 pixels for 30 min and line scans were extracted from the mappings.

3. Results

Here, 12 HAGBs were sampled to analyze the effect of grain boundary structure on the intergranular oxidation behavior of Alloy 600. Except for misorientation, GB plane indexes of all the sampled boundaries were also obtained using a new FIB-EBSD method developed

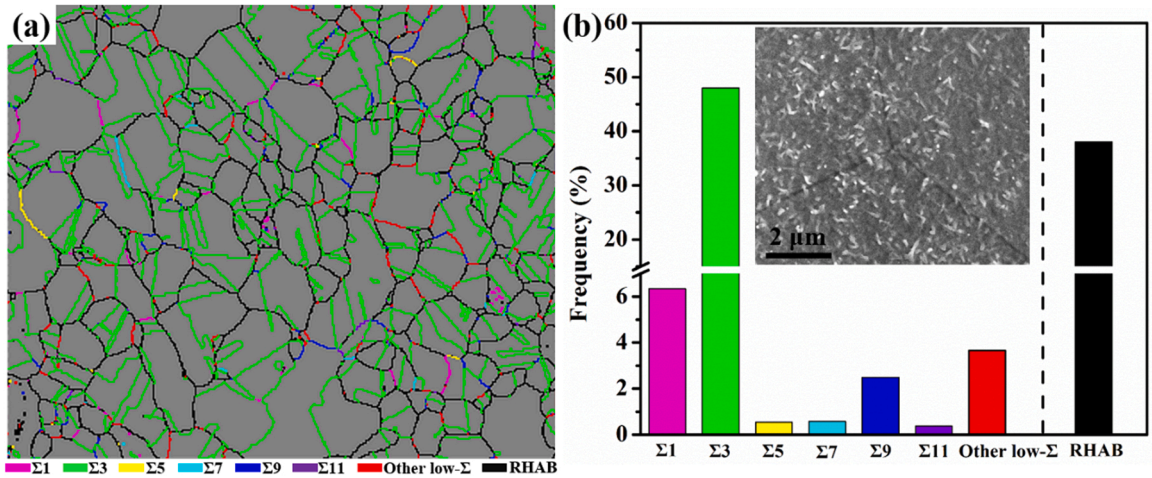

Fig. 1. (a) Grain boundary distribution, (b) the frequency of different types of grain boundaries. The insert shows the typically oxidized surface after oxidation test.

in this group [41]. The accuracy of this technique is better than 3°. To study the microstructure of GB oxidation, all GBs were tilted to edge-on condition in microscope. Table 1 summarizes the grain boundary structure parameters and the extent of intergranular degradation in this study. It should be noted that the measurements of PIO and diffusion-induced grain boundary migration (DIGM) were based on 2D images. 3D imaging technique such as serial FIB/SEM [42] would be a better option if the resource is available. According to the GB oxidation behavior, those boundaries can be divided into three categories.

3.1. CTB

Fig. 2a shows a bright field image of the cross section of a CTB (Σ3-1). The selected area diffraction pattern (SADP) in Fig. 2b shows that the GB trace is parallel to the common (111) plane when the zone axis is tilted to <110> direction. The FIB-EBSD method was applied on the twin boundary and the GB plane normals can be calculated, as shown in Fig. 2c. The $(1\ -1\ 1)_{\sim 3.59^\circ}$ //$(-\ 1\ 1\ 1)_{\sim 2.80^\circ}$ GB plane normals confirm that the twin boundary is a CTB. Fig. 2d shows a STEM-HAADF image of this boundary. The corresponding EDS mapping of O in Fig. 2e indicates that this GB was not oxidized. The EDS line scan (Fig. 2f) taken along the corresponding arrow in Fig. 2d further confirms that the boundary is immune to oxidation. It should be noted that the oxygen concentration from EDS measurement is semi-quantitative.

3.2. ITB and Σ9 boundary

Fig. 3a shows the BF image of an ITB (ITB-1). The SADP from this boundary shows the <110> zone axis of the right grain is parallel to the <114> zone axis of the left grain. The GB trace is straight but not parallel to the common [220]* direction, indicating that this twin boundary is incoherent. Subsequently, the GB plane normals were calculated to be $(1\ -1\ 1)_{\sim 1.74^\circ}$ //$(-\ 1\ 5\ 1)_{\sim 1.73^\circ}$, as shown in Fig. 3b, confirming that this boundary is an ITB. Fig. 3c shows the STEM-HAADF image of this boundary. Different from CTB, this GB was oxidized. The PIO depth was measured to be 546 nm. The EDS maps of O, Ni, Cr, and Fe show that the thin intergranular oxide was Cr-rich oxide and there is no apparent variation in chemical composition beyond the oxide tip. Two quantitative EDS line profiles were extracted across the oxidized GB and the oxide front, as shown in Fig. 3h and i. From Fig. 3h, the intergranular oxide is depleted in Ni and Fe while enriched in Cr and O. However, the EDS line profile beyond the oxide tip shows that there is no significant variation in chemical composition near GB compared to the adjacent matrix (Fig. 3i).

Fig. 4a shows the STEM-HAADF image of Σ9 (Σ9-1) boundary which has a misorientation angle/axis of 38.57°/[− 1 0 1]. The GB plane normals of this boundary were determined to be $(1\ -5\ 1)_{\sim 2.14^\circ}$//$(1\ -\ 1\ 1)_{\sim 2.66^\circ}$ (Fig. 4b) which is the same as the above ITB. From Fig. 4a, the intergranular oxide penetration follows the GB and the PIO depth is around 285 nm. The EDS maps (Fig. 4c–g) show that the intergranular oxide is also Cr-enriched. In addition, there is a Cr and Fe-depleted but Ni-enriched region beyond the oxide tip. The EDS line profile across the intergranular oxide indicates that the oxide is depleted in Ni and Fe but slightly enriched in Cr (Fig. 4h). Moreover, the Cr-rich oxide is next to the left (111) GB plane normal. The EDS line profile across the boundary beyond the oxide tip shows depletion of Cr and Fe and enrichment of Ni (Fig. 4i). The length of Cr-depleted GB region was measured to be 36 nm. Compared with ITB-1, the Σ9-1 boundary shows apparent faster Cr diffusivity. The element composition changes gradually from the matrix to boundary and the width of Cr-depleted region is less than 5 nm. Thus, the limited Cr diffusivity could not induce GB migration. Similar oxidation behavior has been found in LAGB with misorientation below 8.8° [38].

3.3. Σ5 and Σ7 boundary

Fig. 5a shows the STEM-HAADF image of Σ5 (Σ5-1) boundary with a misorientation angle/axis of 37.38°/[0 4 1]. The GB plane indexes were determined to be $(5\ -\ 5\ 7)_{\sim 2.93^\circ}$//$(7\ 5\ 3)_{\sim 1.38^\circ}$, as shown in the crystallographic unit triangle (Fig. 5b). As confirmed by the EDS map of O (inset in Fig. 5a), the PIO depth is 1048 nm, which is much deeper than those in ITB and Σ9 GB. Fig. 5c shows the enlarged image of oxidation tip. The boundary beyond the intergranular oxide is brighter than adjacent matrix, indicating Ni is enriched therein. From the EDS maps, the bright area corresponds to the Cr, Fe-depleted but Ni-enriched DIGM zone, which has been widely observed in Alloy 600 [10,38,43,44] and Alloy 690 [26,45,46]. Due to its higher average Z number, the migration zone appears brighter than matrix in HAADF. Different from ITB and Σ9–1, the formation of DIGM zone suggests that this GB can support rapid diffusion of Cr and Fe. The original and migrated GBs were denoted by white arrows, and the migrated direction was indicated by a yellow arrow in Fig. 5e. From Fig. 5d–g, PIO developed preferentially along the new migrated GB. Moreover, the intergranular oxide is Cr-enriched, which is confirmed by EDS line profile along arrow h in Fig. 5c. Fig. 5i shows the quantitative chemical changes along arrow i which is across the migration zone in Fig. 5c. From the profile, the Ni element is up to 85 at.%, while Cr and Fe are 7 at.% and 6 at.%, respectively. From the EDS maps in Fig. 5c–g, the DIGM zone extends to 345 nm long.

The under-focus bright field image of Σ7 boundary shows some facets along this boundary, as indicated by the yellow arrows in Fig. 6a. From the STEM-HAADF image, the boundary shows serious oxidation and the oxidation depth extends to 900 nm (Fig. 6b). This boundary has a misorientation angle/axis of 41.50°/[− 1 1 1] and the "average" GB plane indexes can be described as $(-\ 6\ 7\ -4)_{\sim 1.47^\circ}$//$(3\ -\ 3\ -\ 2)_{\sim 2.35^\circ}$, as shown in Fig. 6c. From the oxidized GB (Fig. 6b), the intergranular oxidation exhibits non-uniform width. The EDS maps from rectangle region in Fig. 6b show that the distribution of alloying elements in

Table 1
Summary of the high-angle grain boundary crystallographic orientation and the extent of intergranular degradation. Grain boundaries were extracted and analyzed from 7 different types of HAGB.

Sample	GB	Misorientation angle/Axis	GB plane combination	GBAPD	DIGM depth (nm)	Oxidation depth (nm)
1	Σ3-1	59.67°/[− 1 1 1]	$(1\ -1\ 1)_{\sim 3.59^\circ}$//$(-1\ 1\ 1)_{\sim 2.80^\circ}$	0.905	None	0
2	Σ3-2	59.52°/[− 1 1 1]	$(1\ -1\ -\ 1)_{\sim 6.19^\circ}$//$(-\ 1\ 1\ -\ 1)_{\sim 7.36^\circ}$	0.897	None	194
3	Σ3-3	59.94°/[1 1 − 1]	$(1\ -1\ 1)_{\sim 1.74^\circ}$//$(-\ 1\ 5\ 1)_{\sim 1.73^\circ}$	0.823	None	546
4	Σ3-4	59.90°/[− 1 1 − 1]	$(1\ 1\ 1)_{\sim 2.82^\circ}$//$(-\ 1\ 1\ 5)_{\sim 2.87^\circ}$	0.823	None	635
5	Σ5-1	37.38°/[0 4 1]	$(5\ -\ 5\ 7)_{\sim 2.93^\circ}$//$(7\ 5\ 3)_{\sim 1.38^\circ}$	0.842	345	1048
6	Σ5-2	35.47°/[0 4 1]	$(5\ -\ 1\ 3)_{\sim 1.58^\circ}$//$(3\ 8\ 3)_{\sim 1.09^\circ}$	0.724	652	1384
7	Σ7	41.50°/[− 1 1 1]	$(-\ 6\ 7\ -4)_{\sim 1.47^\circ}$//$(3\ -\ 3\ -\ 2)_{\sim 2.35^\circ}$	0.873	782	900
8	Σ9-1	38.57°/[− 1 0 1]	$(1\ -\ 5\ 1)_{\sim 2.14^\circ}$//$(1\ -\ 1\ 1)_{\sim 2.66^\circ}$	0.830	None	285
9	Σ9-2	38.89°/[0 − 1 − 1]	$(-3\ -\ 1\ -\ 1)_{\sim 2.84^\circ}$//$(-\ 1\ -\ 1\ 0)_{\sim 3.80^\circ}$	0.686	468	1015
10	Σ11	50.28°/[1 0 1]	$(-\ 5\ 2\ 8)_{\sim 2.93^\circ}$//$(-\ 1\ 3\ 0)_{\sim 2.44^\circ}$	0.746	396	462
11	RHAB-1	48.67°/[− 3 − 2 − 1]	$(8\ -\ 5\ -\ 2)_{\sim 2.65^\circ}$//$(-\ 1\ -\ 1\ 0)_{\sim 3.25^\circ}$	0.678	1097	1737
12	RHAB-2	35.68°/[− 3 − 2 − 1]	$(-\ 6\ 6\ 1)_{\sim 2.80^\circ}$//$(5\ -\ 8\ -\ 2)_{\sim 1.84^\circ}$	0.690	None	670

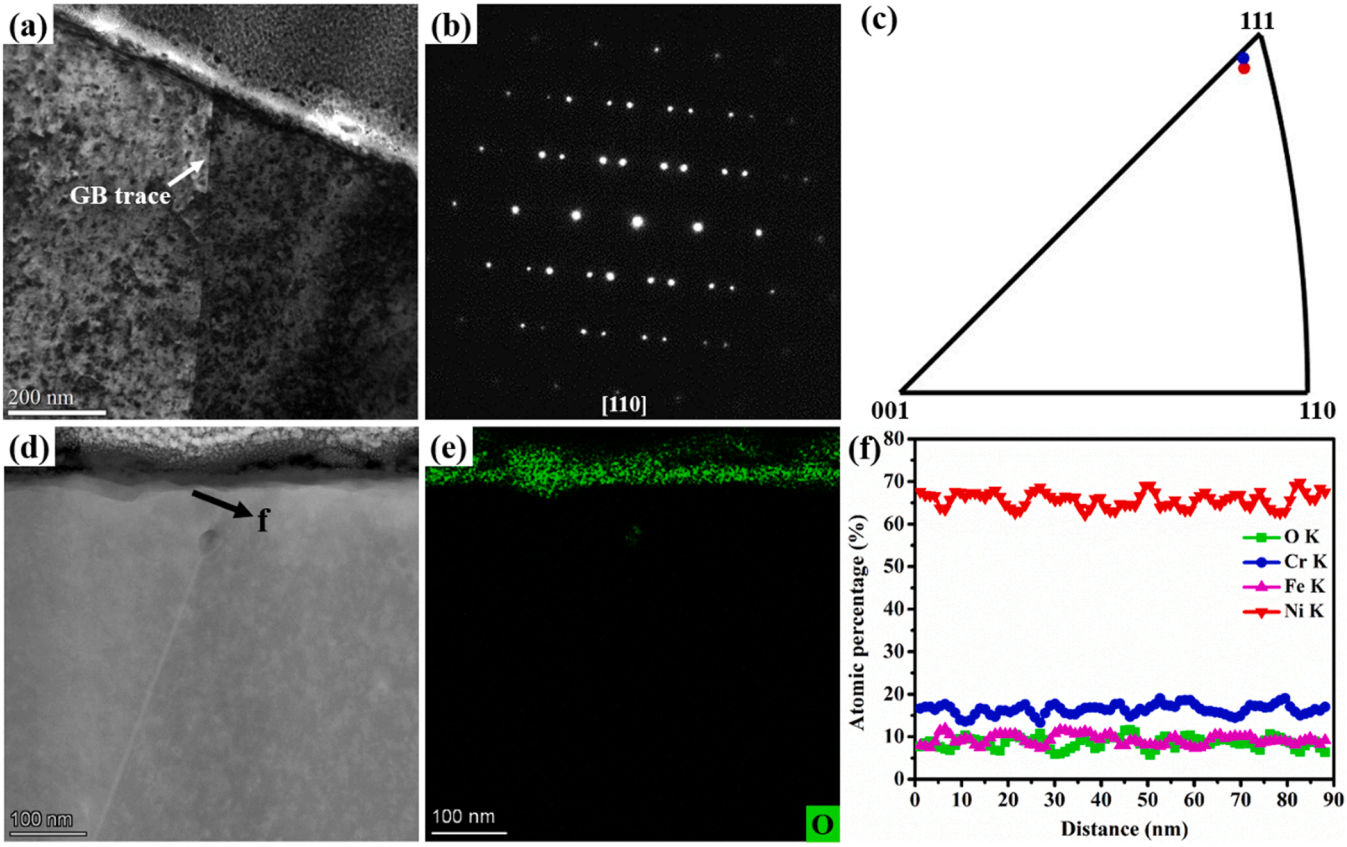

Fig. 2. The oxidation behavior of CTB-1. (a, b) Bright field (BF) image and selected area diffraction pattern (SADP) of CTB-1, (c) the calculated GB plane orientations, where left and right GB planes are labeled by red and blue dots respectively, (d, e) HADDF image and EDS mapping of O, (f) EDS line profile along arrow f in (d).

intergranular oxides is also not uniform (Fig. 6d–g). The oxide near the left grain is Ni and Fe-enriched, while the oxide close to the right grain is Cr-enriched, as indicated in overlapped elemental maps (Fig. 6h and i). The EDS line profile also confirms this asymmetric element distribution in intergranular oxide (Fig. 6j). Tsai et al. [47] also reported the faceted characteristics of Σ7 boundaries in the intergranular corrosion test of 316 stainless steel.

Fig. 7a shows the enlarged image from the oxidation tip in Fig. 6b. From the EDS maps of O, Ni, Cr and Fe, the oxide mainly contains Cr and O (Fig. 7b–e) which is mixed with Ni rich flake. There is a noticeable wide and bright area beneath the intergranular oxide (Fig. 7a). From the EDS maps, the bright area corresponds to the DIGM zone. The large DIGM zone suggests that this boundary can support rapid Cr diffusion during oxidation. The migrated GB, original GB and PIO were denoted by white arrows, and the migration direction was indicated by a yellow arrow in Fig. 7c. To examine the microchemistry of oxidation tip, two EDS line profiles along arrow f and g were taken (Fig. 7a). Fig. 7f shows that the intergranular oxide is Cr-enriched and contains a Ni-enriched flake. Similar feature has been observed in LAGB of Alloy 600 [38]. The EDS line profile across the DIGM zone shows that the region is significantly enriched in Ni and depleted in Cr. The element profile is fairly constant across the region and the depth of DIGM zone was measured to be 782 nm.

For Σ7 boundary, the phase structure of intergranular oxide was analyzed in TEM. Fig. 8a shows the under-focus bright field image. The diffraction pattern from the circled area in Fig. 8a is shown in Fig. 8b with the left substrate tilted to [110] zone axis. The indexed results of diffraction pattern were shown in Fig. 8c. The dark field images of the oxide taken from the numbered spots in Fig. 8c are shown in Fig. 8d-f. The result shows that the intergranular oxide is composed of spinel, NiO and corundum structure oxides. The spinel and NiO has a cube-on-cube relationship with the matrix, and corundum has a rigid orientation relationship with the matrix as reported in [45,46,48]: Cr_2O_3 {006}//substrate {111}, Cr_2O_3 <210>//substrate <110>.

4. Discussion

The intergranular degradation results show that the degree of PIO and solute diffusivity are quite different among the sampled GBs. In order to determine the dependence of PIO tendency on GB structure, the structures of sampled GBs were fully characterized. In this paper, the whole GB structure parameters, including misorientation angle and GB plane normal, have been determined based on the surface EBSD data and GB trace angles using the technique developed before [41]. As the calculated GB plane normal are not necessarily integer, the plane index was represented by the closest integer and the deviation.

The atom packing density (APD) was calculated from the GB plane index as it may be directly related to the performance of GB. The APD of GB plane is defined by the ratio of atom occupied area to the corresponding plane area and its value reflects how dense an arbitrary plane is packed [49]. A Monte Carlo method was employed to calculate the APD value of GB plane. The calculation principle has been described in detail by Wang [49]. In general, a large number of dots were uniformly projected onto the target crystal plane in a face-centered cubic (FCC) unit cell. The number of dots within the atom-occupied area was counted and the ratio of this number to the total dot number is the APD value of target plane. The grain boundary atom packing density (GBAPD), which can be expressed as the average of the APD values of the two coupling GB planes, is used here. Boundaries with low GBAPD values tend to have less atoms on two GB planes, so less bonds would be made between two adjacent GB planes and the disordered boundaries offer more space for solute atom and oxygen transport [40,49].

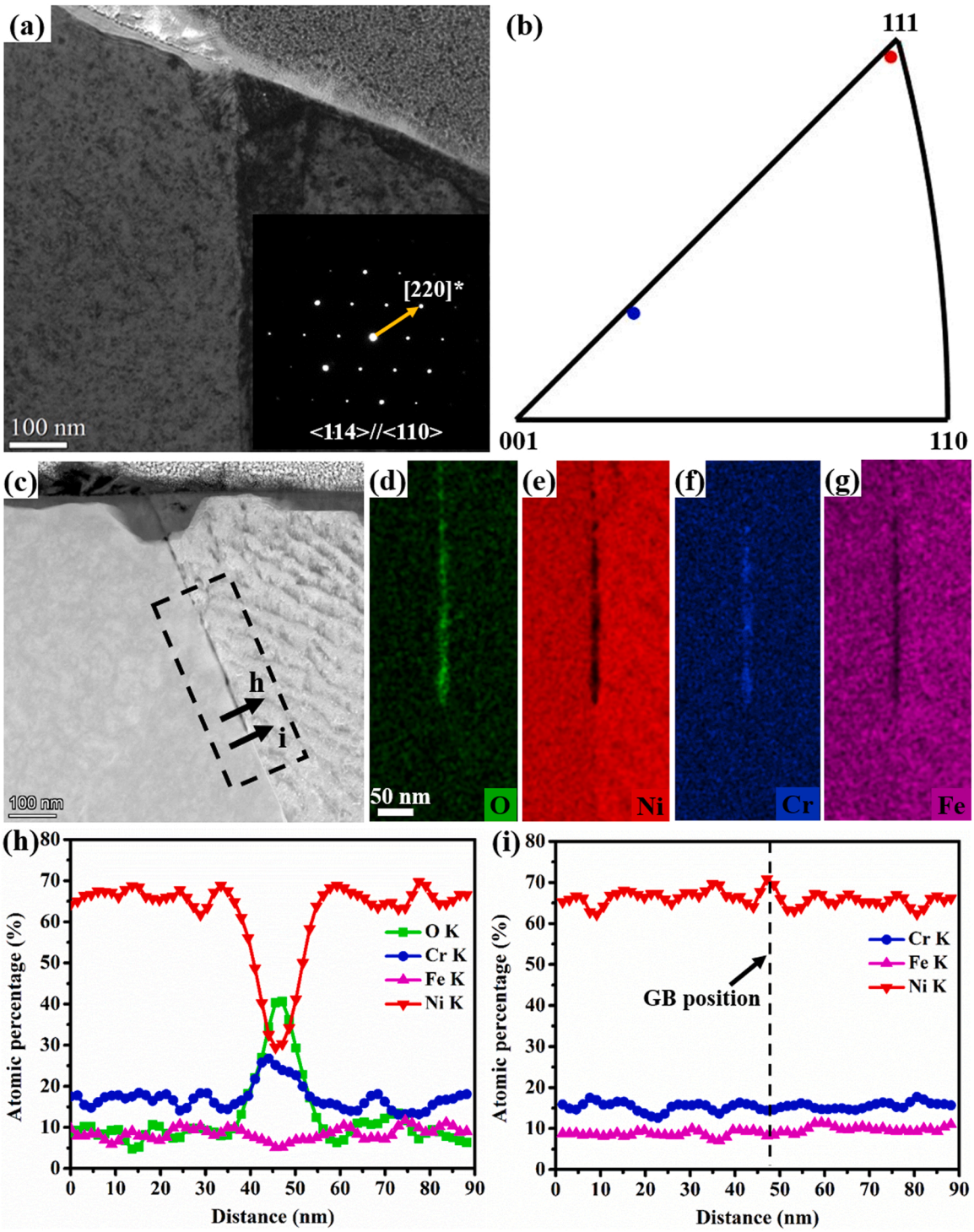

Fig. 3. The oxidation behavior of ITB-1. (a) Bright field (BF) image and selected area diffraction pattern (SADP) of ITB-1, (b) the GB plane orientation distribution, where left and right GB planes are respectively labeled by red and blue dots, (c–g) HADDF image and associated EDS mapping of O, Ni, Cr and Fe, (h and i) EDS line profiles along arrow h and i in (c).

4.1. Dependence of PIO on GB type

PIO is an important precursor event in the SCC initiation process [13,14,46,50–52] and DIGM is closely related to PIO [10,43,44,53]. In our previous work [38], it was found that GBAPD plays a more important role in GB degradation behavior than misorientation angle for LAGB with misorientation angle larger than 8.8°. Whether this conclusion apply to HAGB should be further verified.

Table 1 summarizes the GB structure parameters and the extent of intergranular degradation in this study. All HAGBs were oxidized except for the ideal CTB (CTB-1). This CTB behaves completely differently from other HAGBs. There is no signs of long-range diffusion of Cr and the oxygen ingress was completely suppressed in CTB-1 (Fig. 2). The immunity of CTB to intergranular degradation behavior is mainly due to the highly-ordered boundary structure. Consistent results have also been reported by Lim et al. [30].

It should be noted that another CTB that deviates from perfect coherency (CTB-2) was oxidized (Table 1). Thus, when the GB coherency is

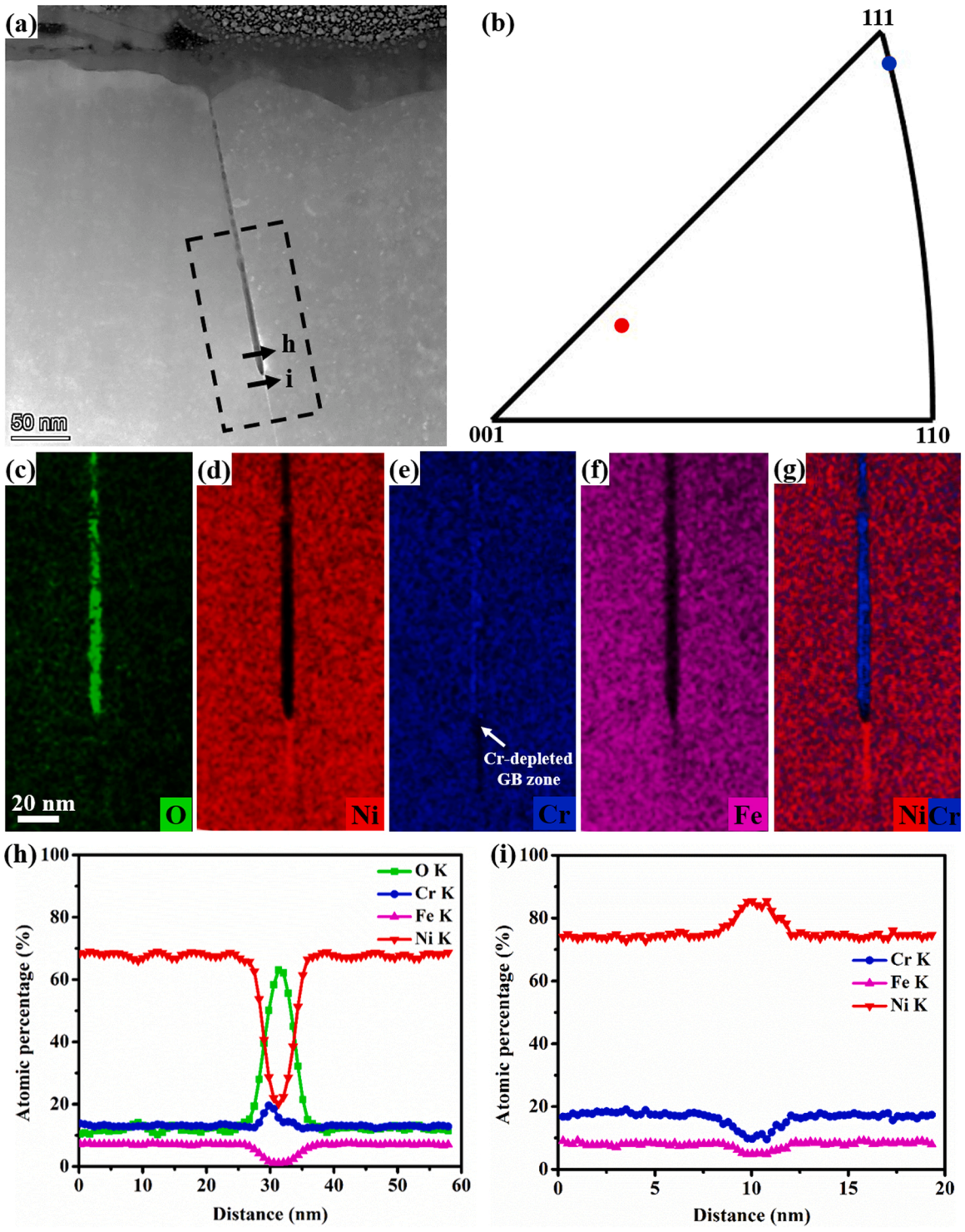

Fig. 4. The oxidation behavior of Σ9-1. (a) HADDF image of Σ9-1, (b) the GB plane orientation distribution, where left and right GB planes are respectively labeled by red and blue dots, (c–f) HADDF image and associated EDS mapping of O, Ni, Cr, Fe and (g) overlap mapping of Ni and Cr, (h and i) EDS line profiles along arrow h and i in (a).

compromised, oxygen ingress occurs along the boundary which leads to slight oxidation on CTB-2. As the GB coherency further decreases in ITB, the oxygen diffusivity was enhanced and the PIO was further accelerated (Fig. 3). There is almost no sign of Cr depletion beyond the intergranular oxide tip in CTB-2 as well as in the other two ITBs, indicating that Cr is nearly immobile along twin boundaries (including CTB and ITB) at this temperature. The oxidation behavior of those twin boundaries is similar to that of LAGBs with misorientation angle smaller than 8.8° [38]. Σ9-1 boundary exhibits a similar oxidation behavior as ITB (Fig. 4). The PIO is shallow and there is no sign of GB migration although a short Cr-depleted region formed beyond the oxide tip, indicating very limited Cr diffusion along GB. Overall, the above GBs show no or limited Cr diffusion and are subject to mild intergranular oxidation except that ideal CTB is immune to oxidation.

The rest GBs are more susceptible to intergranular oxidation. A typical feature of these GBs is that they could support fast Cr diffusion

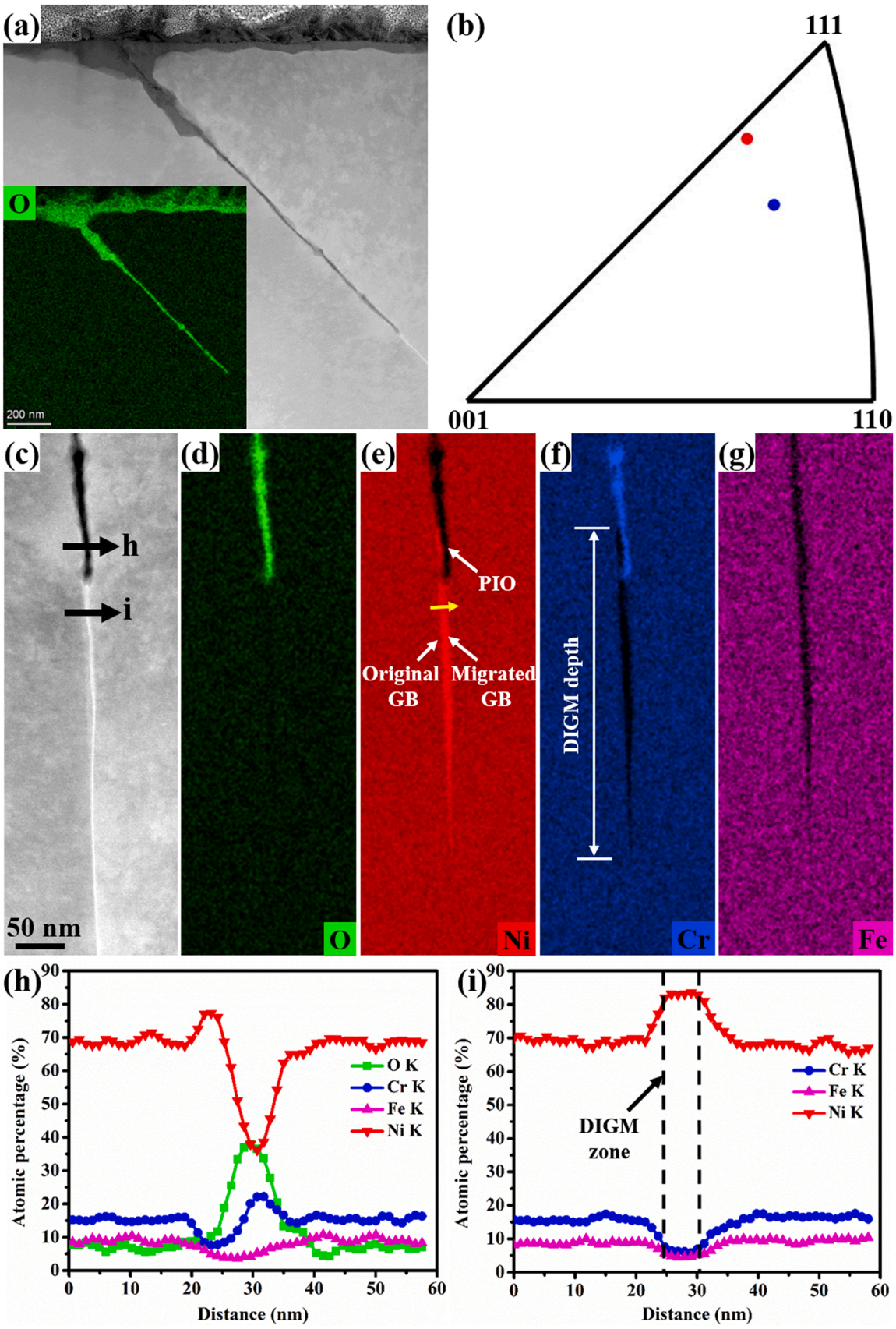

Fig. 5. The oxidation behavior of Σ5-1. (a) HADDF image and EDS mapping of O, (b) the GB plane orientation distribution, where left and right GB planes are respectively labeled by red and blue dots, (c) enlarged image of the oxidation tip, (d–g) EDS mapping of O, Ni, Cr and Fe, (h, i) EDS line profiles along arrow h and i in (c).

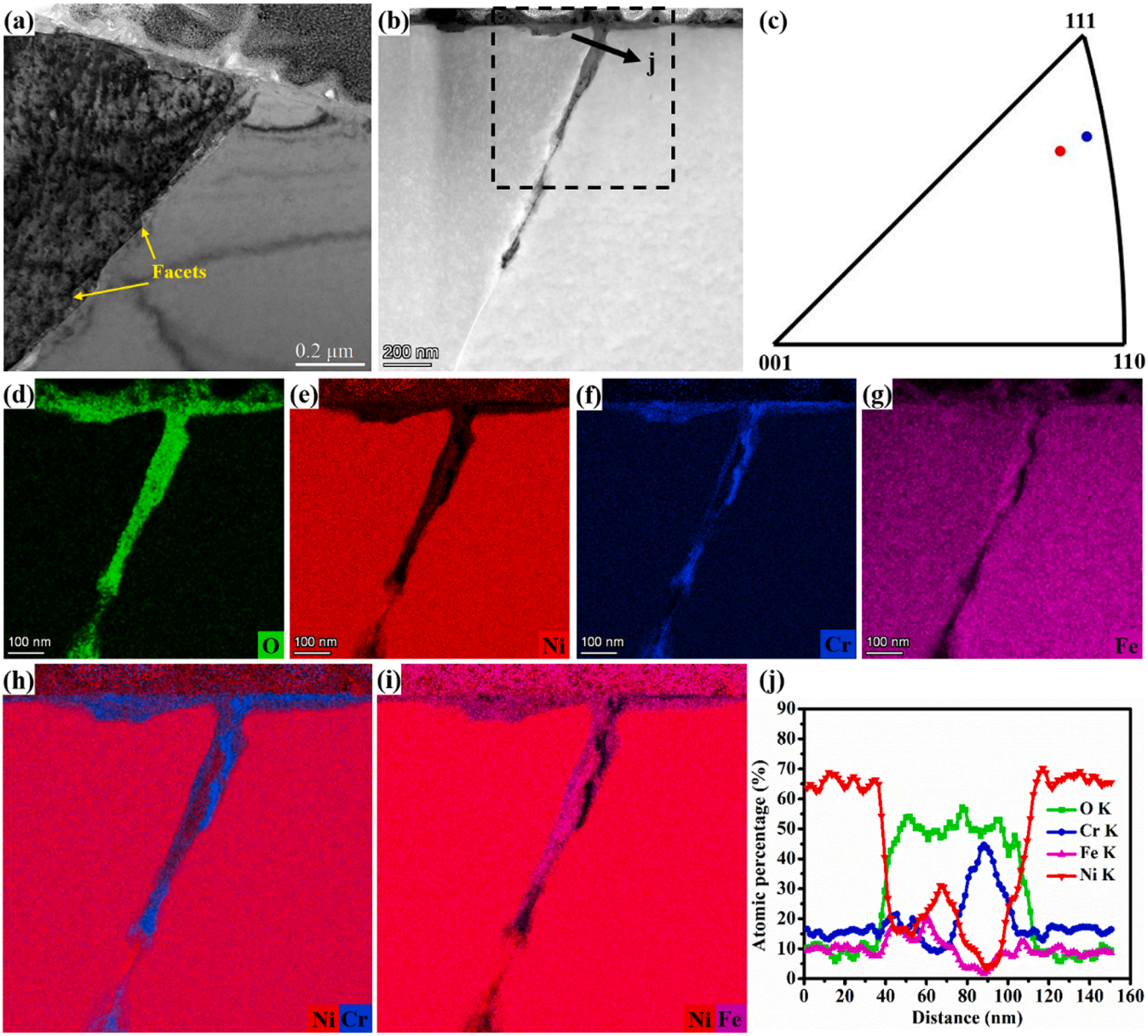

Fig. 6. The oxidation behavior of Σ7. (a) Under-focus TEM image of Σ7, (b) STEM-HAADF image, (c) the GB plane orientation distribution, where left and right GB planes are respectively labeled by red and blue dots, (d–g) EDS mapping of O, Ni, Cr and Fe, (h, i) overlap mapping of (Cr, Ni) and (Fe, Ni), (j) EDS line profile along arrow j in (b).

and DIGM occurred in Σ5 (Fig. 5) and Σ7 (Fig. 7). DIGM has been widely reported in Alloy 600 after exposure in simulated PWR primary water [38,51,53] and high temperature steam [10,43,44,50]. The depth of DIGM zone can be used to reflect the diffusivity of solute atom (such as Cr) along GB. Our previous work suggests that the depths of PIO and DIGM zone are positively correlated for LAGB with misorientation angle larger than 8.8° [38]. Fig. 9 shows the relationship between PIO and DIGM depths for the sampled HAGBs. The data from LAGBs [38] was also included. Some HAGB (sample 12 in Table 1) was oxidized even in the absence of DIGM. So DIGM is not essential for the occurrence of PIO. Nevertheless, the PIO depth generally increases with increasing DIGM depth. Given that PIO is dictated by oxygen ingress and DIGM is controlled by Cr diffusion, it seems that the diffusivities of solute atom and oxygen along a single boundary are positively correlated in this alloy.

Fig. 10a and b show the variations of DIGM depth over misorientation angle and Σ value. The random distribution of dots suggests that the solute diffusivity is not directly related to either misorientation angle or Σ value for HAGB. For instance, the two Σ9 boundaries exhibit completely different solute diffusivities, even though they have the same misorientation angle/axis and Σ value. The two Σ5 boundaries also behave quite differently. Similarly, there is no clear relationship between PIO extent and misorientation angle or Σ value, suggesting that the susceptibility to PIO is independent on misorientation angle or Σ value (Fig. 10c and d). Fujii et al. [54,55] studied the relationship between intergranular corrosion (IGC) susceptibility and Σ value and also demonstrated that the IGC area did not depend on the Σ value. More importantly, one RHAB even shows much shallower PIO depth than some CSL GBs (Fig. 9). Therefore, the resistance to PIO of GB probably can't be reflected from the GB classification based on CSL concept.

4.2. *Effect of GB plane on PIO*

The solute diffusivity along the boundary and the intergranular

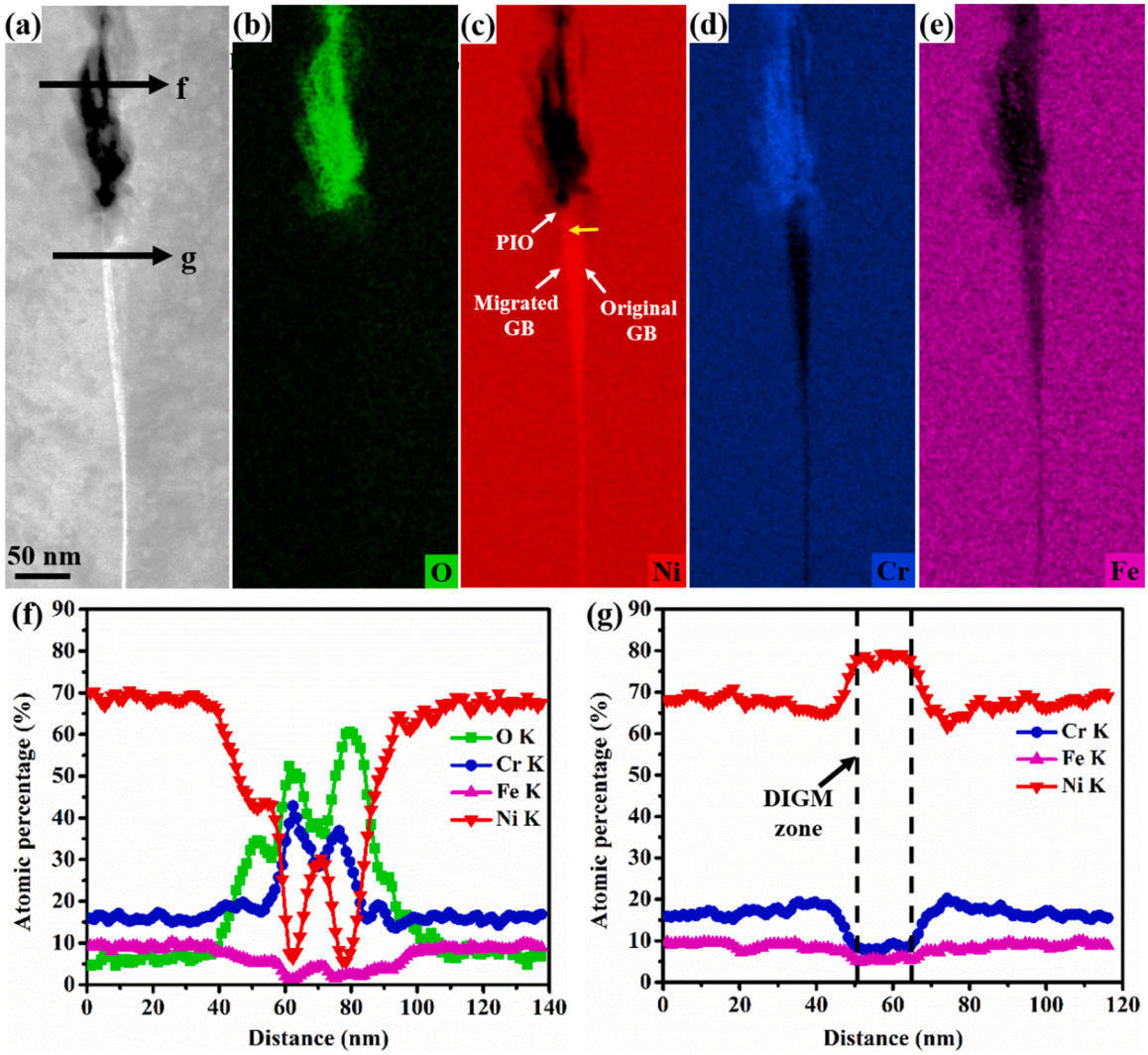

Fig. 7. (a) HADDF image of oxidation tip of Σ7, (b–e) EDS mapping of O, Ni, Cr and Fe, (f and g) EDS line profiles along arrow f and g in (a).

oxidation process should be dictated by some factors other than misorientation angle or CSL Σ value. Recently, Kuang and Was [26] and Minkwitz et al. [39] found that the solute diffusivity along Σ3 boundary was strongly affected by the density of coincident site in grain boundary plane. However, the key factors that dictate properties of other HAGB are still unknown. Our recent work [38] indicates that GB plane orientation plays an important role on solute diffusivity and intergranular degradation in LAGB when the misorientation angle is above 8.8°. Whether the GB plane also plays a dominant role on solute diffusivity and PIO process in HAGBs needs to be further verified.

Previous work shows that the GB plane orientation has a strong effect on GB properties such as GB diffusion [26,39], migration [56], intergranular corrosion [40,47], segregation and fracture [57–59]. The GB with low-index plane tends to exhibit greater degradation resistance. Moreover, some model was proposed to explain the GB degradation behavior [49,60,61]. Miyamoto et al. [61] studied the role of grain boundary plane orientation on intergranular corrosion and reported that there is an inverse linear relation between the susceptibility to intergranular corrosion and "effective interplanar spacing". However, this parameter cannot directly reflect the atomic structure of a specific grain boundary. Recently, GBAPD theory was applied to explain the intergranular corrosion phenomenon in an AISI 304L stainless steel. An and Zaefferer [40] found that the crystallographic orientation of GB plane is a dominant factor in the corrosion behavior of low-Σ CSL GBs and RHABs.

Fig. 11a shows the distribution of PIO depth with the GB plane combinations within the orientation triangle (The background color of orientation triangle represents the APD of the corresponding GB plane, and the color of circles represents the PIO depth). From Fig. 11a, the PIO depth increases as the APD of GB plane decreases. It is noticed that the GBs comprising one (1 1 1) plane such as two ITB and Σ9–1 shows a higher oxidation resistance than other boundaries. That is probably because those boundaries have higher GBAPD and less space [40] and lower GB energies [62] hinder solute atom and oxygen diffusion along GBs. As the GB plane deviates from the (1 1 1) orientation, the solute diffusivity increases. Given that the spinel oxide cannot prevent further oxidation of the grain boundaries below (Fig. 8), the PIO susceptibility was enhanced. Particularly, the Σ7 boundary shows a high PIO susceptibility although it has a high GBAPD, suggesting some factors other than GB plane orientation also affect the solute diffusivity. The unusual behavior of Σ7 might be due to its facet character caused by the strong GB energy anisotropy [47]. Some previous studies used the grain boundary serration (GBS) to explain GB faceting in Ni-based alloy [63–65] and stainless steel [66]. The GBS theory suggests that the formation of serrated GB is to reduce the total GB energy. The GBs with higher energy tend to be serrated and form specific lower-energy segments [64,66]. The faceted GB changes GB plane orientation, hence the GBAPD value is not constant along the GB. An [40] and Tsai [47] had

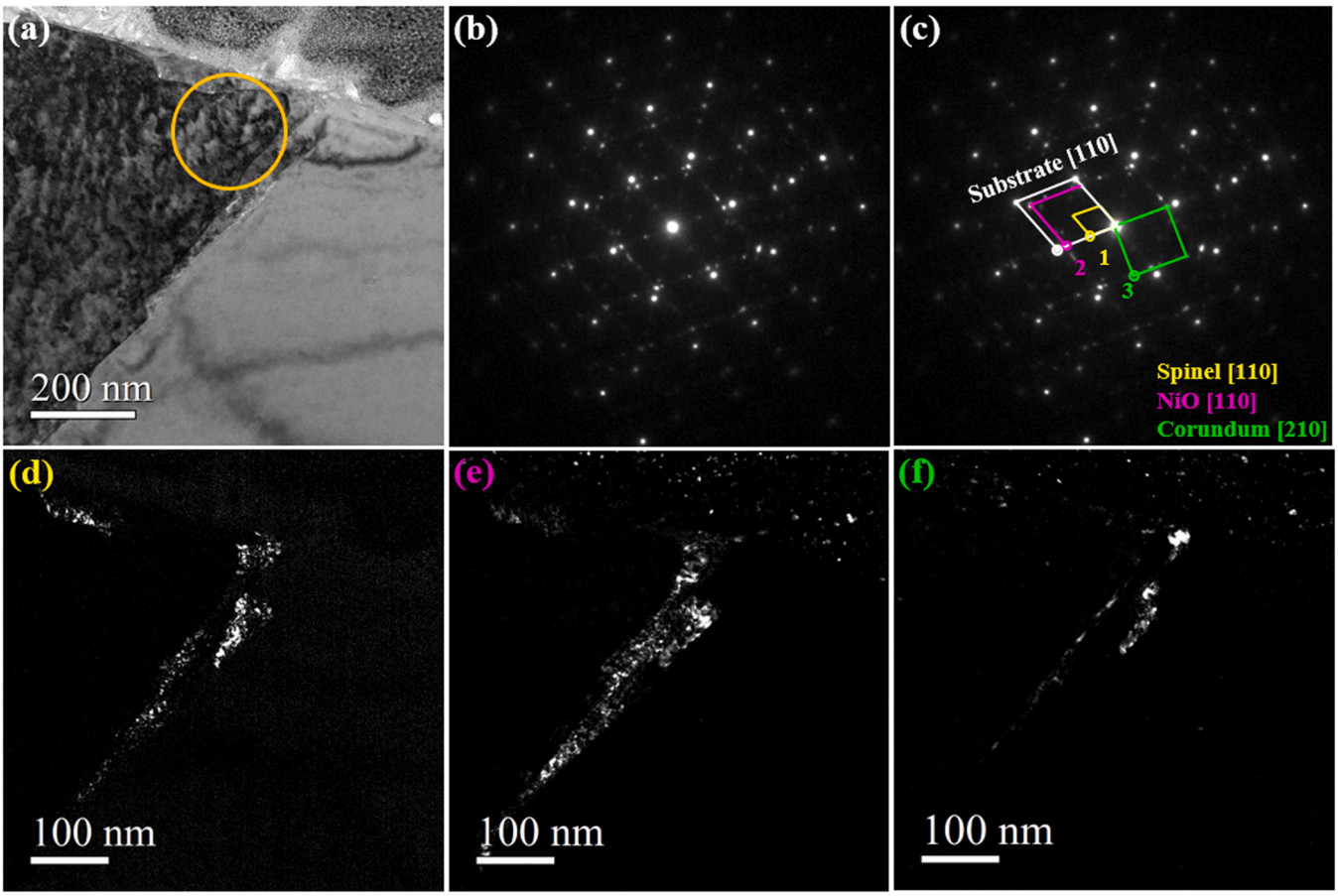

Fig. 8. TEM micrograph of inner and intergranular oxide of Σ7, (b) diffraction pattern of circled area in (a), (c) the indexed results of diffraction pattern in (b), (d–f) dark field (DF) images corresponding to spots 1–3 in (c).

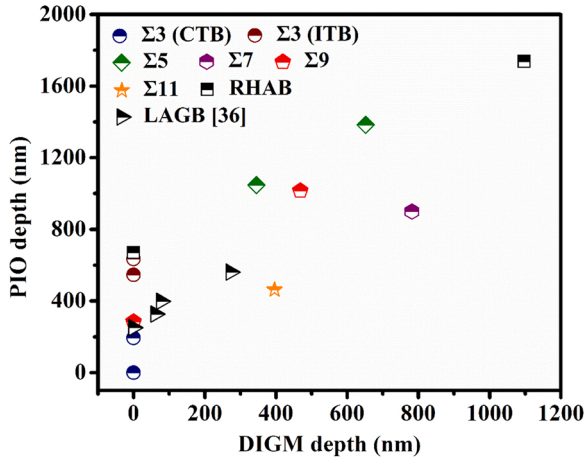

Fig. 9. The relationship between PIO depth and DIGM depth.

also found the unusual behavior of Σ7 boundary, and Tsai further indicated that the stronger GB energy anisotropy (instead of absolute energies) is the main reason for the formation of GB facet. The Σ7 boundary tends to facet into (111) low-indexed plane on at least one side of GB, resulting in faceted GB with higher GBAPD. However, some high-indexed planes also formed during faceting process and support fast diffusion of solute atom along GB. Therefore, the faceted GB exhibits high oxidation susceptibility even when its GBAPD is high.

Fig. 11b shows the correlation between PIO depth and GBAPD. The PIO depth exhibits a decreasing trend with increasing GBAPD. Moreover, the oxidation susceptibility of the same type of GBs decreases with the increase of GBAPD, such as Σ3, Σ5, Σ9 and RHAB. This trend confirms that GB plane orientation is a key factor affecting intergranular oxidation process. Hanson et al. [59] found the GBs with low-index planes, such as {001}, {011} or {111}, show a striking high resistance to hydrogen-assisted crack propagation. Hu et al. [57] reported that the coupling GB planes affect the S adsorption and then determine the sulfur embrittlement of nickel. Despite the relationship between GB plane orientation and degradation properties was reported, a deeper insight into those correlations is still lacking. The present results suggest that the GBAPD affects the intergranular oxidation behavior through controlling the solute diffusivity, and finally determines the oxidation kinetics. Consistent result has also been found in the oxidation behavior of LAGB of Alloy 600 [38]. Based on broken-bond model [67,68], the GBs can be considered as a combination of two GB planes. GBs with higher GBAPD tend to form more coordination bonds between the two GB planes. The formation of bonds between the two adjacent GB planes hinders the diffusion of solute atoms and oxygen along GBs. Moreover, extensive work suggests that the GB energy tends to decrease as the APD of GB plane increases [62,69–71]. Therefore, the GB plane is the key factor for intergranular degradation behavior of Alloy 600 in high temperature water. The present work confirms that GBAPD theory applies to relatively straight boundaries although it cannot precisely reflect the atomic packing density for faceted or curved boundaries due to their changed GB plane orientation.

5. Conclusions

The present study investigated the intergranular oxidation behaviors

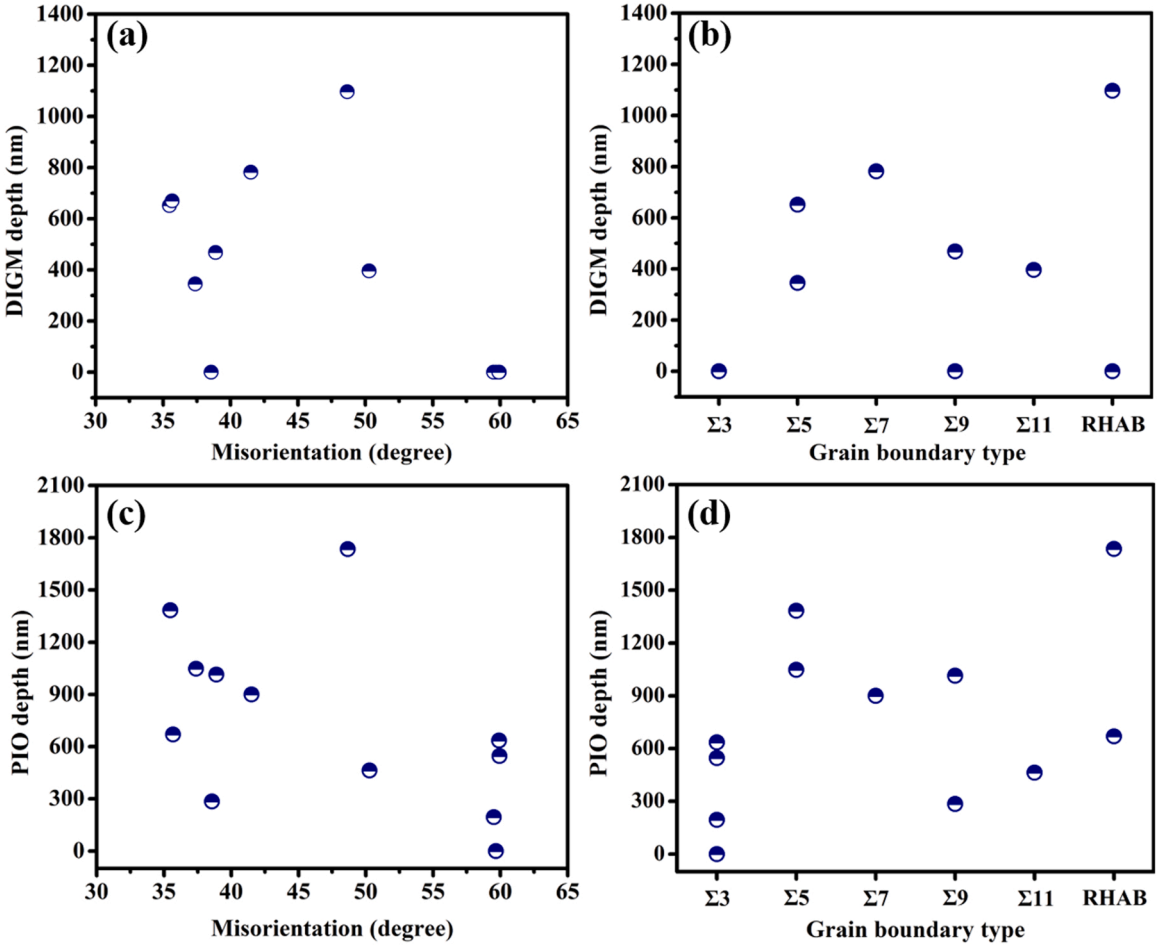

Fig. 10. the changes of DIGM depth and PIO depth as function of misorientation and GB type.

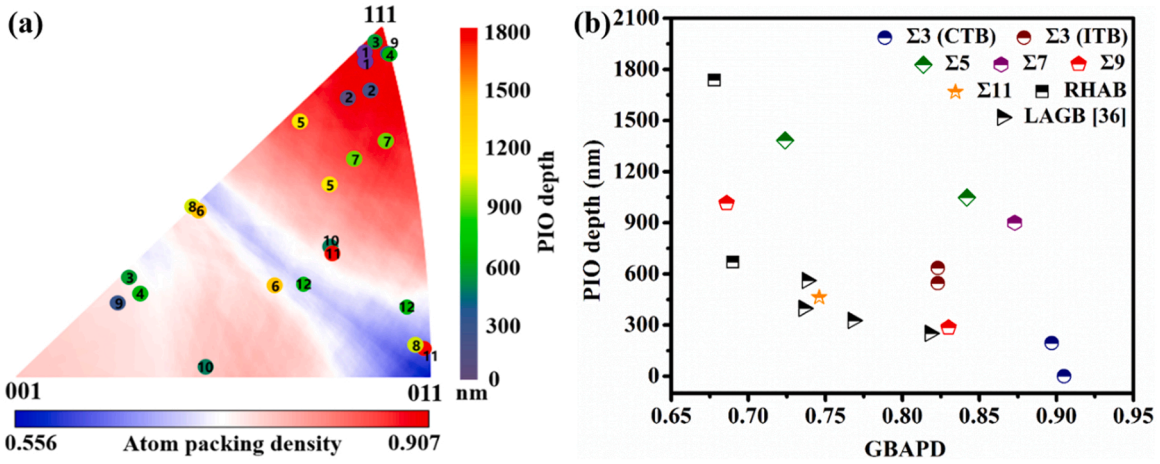

Fig. 11. (a) The distribution of PIO depth with the GB plane orientation. The background color of stereographic projection indicates the atom packing density (APD) of the GB planes. Each solid circle representing plane normal orientation and GB plane pairs belonging to the same GB are denoted by the same number. The colors of solid circles represent the depth of PIO. (b) PIO depth as function of the APD of GB.

of different types of HAGBs of Alloy 600 exposed to simulated PWR primary water. The microstructural and microchemical features of oxidized GBs were studied and correlated with the detailed GB structure. Effects of grain boundary structures on solute diffusivity and intergranular oxidation behavior of HAGBs were analyzed and the following conclusions can be drawn:

1. Regardless of the Σ value, all the sampled grain boundaries were preferentially oxidized except ideal CTB. DIGM normally occurs beyond PIO in HAGBs, but it is not a necessary step for PIO.
2. The GB structure greatly affects the PIO kinetics via controlling the element diffusivity. For Alloy 600, the PIO depth is positively correlated with the DIGM depth, indicating that the transportation

rates of oxygen and solute atoms along GB are similarly dependent on GB structure.
3. Compared with misorientation angle and Σ value, GBAPD is a more important factor in the intergranular degradation behavior of Alloy 600. GB with higher GBAPD tends to be oxidized at a slower rate as the element diffusion is slower.

CRediT authorship contribution statement

Xingyu Feng: Data curation, Investigation, Methodology, Visualization, Writing – review & editing. **Qi Wang:** Data curation, Investigation. **Jiayu Xie:** Methodology, Data curation. **Wenjun Kuang:** Conceptualization, Data curation, Funding acquisition, Investigation, Methodology, Project administration, Supervision, Writing – review & editing.

Declaration of Competing Interest

The authors declare that they have no known competing financial interests or personal relationships that could have appeared to influence the work reported in this paper.

Data Availability

Data will be made available on request.

Acknowledgements

The authors gratefully acknowledge the financial support of the National Natural Science Foundation of China (52271068 and 51971172) and the Young Talent Support Plan of Xi'an Jiaotong University. The authors thank Dr. Chao Li at Instrument Analysis Center of Xi'an Jiaotong University for his assistance with STEM and EDS analysis, and Mingzheng Huang from Xi'an Jiaotong University for helping with the EBSD data analysis.

References

[1] V.Y. Gertsman, S.M. Bruemmer, Study of grain boundary character along intergranular stress corrosion crack paths in austenitic alloys, Acta Mater. 49 (2001) 1589–1598.
[2] H. Coriou, L. Grall, V. LeGall, S. Vettier, Stress Corrosion Cracking of Inconel in High Temperature Water, North Holland Publishing Co., Amsterdam, 1960, pp. 161–169.
[3] R.W. Staehle, J.A. Gorman, Quantitative assessment of submodes of stress corrosion cracking on the secondary side of steam generator tubing in pressurized water reactors: Part 1, Corrosion 59 (2003) 931–994.
[4] R.W. Staehle, J.A. Gorman, Quantitative assessment of submodes of stress corrosion cracking on the secondary side of steam generator tubing in pressurized water reactors: Part 2, Corrosion 60 (2004) 5–63.
[5] R.W. Staehle, J.A. Gorman, Quantitative assessment of submodes of stress corrosion cracking on the secondary side of steam generator tubing in pressurized water reactors: Part 3, Corrosion 60 (2004) 115–180.
[6] P.M. Scott, An overview of internal oxidation as a possible explanation of intergranular stress corrosion cracking of Alloy 600 in PWRs, in: Proceedings of the 9th Int. Conf. Environ. Degrad. Mater. Nucl. Power Syst. — Water React, The Minerals, Metals and Materials Society, Newport Beach, CA, 1999.
[7] P.M. Scott, M.L. Calvar, Some possible mechanisms of intergranular stress corrosion cracking of alloy 600 in PWR primary water, in: Proceedings of the Sixth International Symposium on Environmental Degradation of Materials in Nuclear Power Systems-Water Reactors, San Diego, CA, USA, 1993, pp. 657–65.
[8] R.C. Newman, T.S. Gendron, P.M. Scott, Internal oxidation and embrittlement of alloy 600, in: Proceedings of the Ninth International Symposium on Environmental Degradation of Materials in Nuclear Power Systems-Water Reactors, Newport Beach, CA, USA, 1999.
[9] M.B. Capell, G.S. Was, Selective internal oxidation as a mechanism for intergranular stress corrosion cracking of Ni-Cr-Fe alloys, Metall. Mater. Trans. A 38 (6) (2007) 1244–1259.
[10] G. Bertali, F. Scenini, M.G. Burke, Advanced microstructural characterization of the intergranular oxidation of alloy 600, Corros. Sci. 100 (2015) 474–483.
[11] A. Stratulat, D.E.J. Armstrong, S.G. Roberts, Micro-mechanical measurement of fracture behaviour of individual grain boundaries in Ni alloy 600 exposed to a pressurized water reactor environment, Corros. Sci. 104 (2016) 9–16.
[12] H. Dugdale, D.E.J. Armstrong, E. Tarleton, S.G. Roberts, S. Lozanno-Perez, How oxidized grain boundaries fail, Acta Mater. 61 (2013) 4707–4713.
[13] L. Fournier, O. Calonne, P. Combrade, P. Scott, P. Chou, R. Pathania, Grain boundary oxidation and embrittlement prior to crack initiation in alloy 600 in PWR primary water, in: Proc. of the 15th Int. Conf. on Environmental Degradation of Materials in Nuclear Power Systems-Water Reactor, 2011, pp. 1491–501.
[14] K. Fujii, T. Miura, H. Nishioka, K. Fukuya, Degradation of grain boundary strength by oxidation in alloy 600, in: Proceedings of the 15th International Conference on Environmental Degradation of Materials in Nuclear Power Systems-Water Reactors, Colorado Springs, Colorado, USA, 2011, pp. 1447–58.
[15] M. Kanzaki, Y. Masaki, T. Kudo, Effect of Cr and Ni on stress corrosion cracking susceptibility in Ni-Cr-Fe alloys under simulated pressurized water reactor primary conditions, Corrosion 71 (2015) 1027–1035.
[16] R.P. Matthews, R.D. Knusten, J.E. Westraadt, T. Couvant, Intergranular oxidation of 316L stainless steel in the PWR primary water environment, Corros. Sci. 125 (2017) 175–183.
[17] M. Meisnar, M. Moody, S. Lozano-Perez, Atom probe tomography of stress corrosion crack tips in SUS316 stainless steels, Corros. Sci. 98 (2015) 661–671.
[18] S. Lozano-Perez, K. Kruska, I. Iyengar, T. Terachi, T. Yamada, The role of cold work and applied stress on surface oxidation of 304 stainless steel, Corros. Sci. 56 (2012) 78–85.
[19] K. Kruska, S. Lozano-Perez, D.W. Saxey, T. Terachi, T. Yamada, G.D.W. Smith, Nanoscale characterisation of grain boundary oxidation in cold-worked stainless steels, Corros. Sci. 63 (2012) 225–233.
[20] J. Xie, S. Zhang, J. Dong, S. Wang, H. Wang, W. Kuang, Insights into the superior stress corrosion cracking resistance of FeCrAl alloy in high temperature hydrogenated water: the critical role of grain boundary oxidation, Corros. Sci. 208 (2022), 110668.
[21] S. Zhang, S. Wang, X. Feng, Z. Ning, J. Hou, W. Kuang, Insights into the stress corrosion cracking resistance of a selective laser melted 304L stainless steel in high-temperature hydrogenated water, Acta Mater. 244 (2023), 118561.
[22] L. Legras, B. Marylou, F. Elodie, C. Priscille, M. Remi, M. Salem, T. Jinane, R. Menand, TEM investigations of the microstructure and oxides at the tip of intergranular cracks of a baffle former bolt irradiated up to 10 dpa, in: FONTEVRAUD 9, Avignon, France, 2018.
[23] L.E. Thomas, S.M. Bruemmer, Microstructural and microchemical characterization of intergranular stress corrosion cracks in irradiated type 304SS removed from a BWR top guide, in: Proceedings of the 11th Int. Conf. on Environmental Degradation of Materials in Nuclear Power Systems, Stevenson, WA, 2003.
[24] L.E. Thomas, D. Edwards, K. Asano, S. Ooki, S. Bruemmer, Crack-tip characteristics in BWR service components, in: Proceedings of the 13th International Conference on Environmental Degradation of Materials in Nuclear Power Systems, Whistler, British Columbia, 2007.
[25] W. Kuang, X. Feng, D. Du, M. Song, M. Wang, G.S. Was, A high-resolution characterization of irradiation-assisted stress corrosion cracking of proton-irradiated 316L stainless steel in simulated pressurized water reactor primary water, Corros. Sci. 199 (2022), 110187.
[26] W. Kuang, G.S. Was, The effect of grain boundary structure on the intergranular degradation behavior of solution annealed alloy 690 in high temperature, hydrogenated water, Acta Mater. 182 (2020) 120–130.
[27] W. Kuang, G.S. Was, C. Miller, M. Kaufman, T. Alam, B. Gwalani, R. Banerjee, The effect of cold rolling on grain boundary structure and stress corrosion cracking susceptibility of twins in alloy 690 in simulated pressurized water reactor primary environment, Corros. Sci. 130 (2018) 126–137.
[28] S. Yamaura, Y. Igarashi, S. Tsurekawa, T. Watanabe, Structure-dependent intergranular oxidation in Ni–Fe polycrystalline alloy, Acta Mater. 47 (1999) 1163–1174.
[29] B. Alexandreanu, B. Capell, G.S. Was, Combined effect of special grain boundaries and grain boundary carbides on IGSCC of Ni-16Cr-9Fe-xC alloys, Mater. Sci. Eng. A 300 (2001) 94–104.
[30] Y.S. Lim, S.W. Kim, S.S. Hwang, H.P. Kim, C. Jang, Intergranular oxidation of Ni-based Alloy 600 in a simulated PWR primary water environment, Corros. Sci. 108 (2016) 125–133.
[31] D.C. Crawford, G.S. Was, The role of grain boundary misorientation in intergranular cracking of Ni-16Cr-9Fe in 360 ℃ argon and high-purity water, Metall. Trans. A 23A (1992) 1195–1206.
[32] A. King, G. Johnson, D. Engelberg, W. Ludwig, J. Marrow, Observations of intergranular stress corrosion cracking in a grain-mapped polycrystal, Science 321 (2008) 382–385.
[33] K.J. Leonard, M.N. Gussev, J.N. Stevens, J.T. Busby, Analysis of stress corrosion cracking in alloy 718 following commercial reactor exposure, J. Nucl. Mater. 466 (2015) 443–459.
[34] Y. Pan, B.L. Adams, T. Olson, N. Panayotou, Grain-boundary structure effects on intergranular stress corrosion cracking of alloy X-750, Acta Mater. 44 (1996) 4685–4695.
[35] S.L. Yang, U. Krupp, H.J. Christ, V.B. Trindade, The relationship between grain boundary character and the intergranular oxide distribution in IN718 superalloy, Adv. Eng. Mater. 7 (2005) 723–726.
[36] M.P. Phaniraj, D.I. Kim, Y.W. Cho, Effect of grain boundary characteristics on the oxidation behavior of ferritic stainless steel, Corros. Sci. 53 (2011) 4124–4130.
[37] J. Nguejio, J. Crépin, C. Duhamel, F. Gaslain, Catherine Guerre, F. Jomard, M. Maisonneuve, Diffusion processes as possible mechanisms for Cr depletion at SCC crack tip, in: Proceedings of the 18th International Conference on Environmental Degradation of Materials in Nuclear Power Systems - Water Reactors, Portland, Oregon, USA, 2018, pp. 337–57.

[38] X. Feng, J. Xie, M. Huang, W. Kuang, The oxidation behavior of low-angle grain boundary of alloy 600 in simulated pressurized water reactor primary water, Acta Mater. 224 (2022), 117533.
[39] C. Minkwitz, C.H.R. Herzig, E. Rabkin, W. Gust, The inclination dependence of gold tracer diffusion along a Σ3 twin grain boundary in copper, Acta Mater. 47 (1999) 1231–1239.
[40] D. An, T.A. Griffiths, P. Konijnenberg, S. Mandal, Z. Wang, S. Zaefferer, Correlating the five parameter grain boundary character distribution and the intergranular corrosion behaviour of a stainless steel using 3D orientation microscopy based on mechanical polishing serial sectioning, Acta Mater. 156 (2018) 297–309.
[41] X. Feng, J. Xie, W. Kuang, A novel approach to index site-specific grain boundary plane, Mater. Charact. 174 (2021), 110999.
[42] B. Langelier, S.Y. Persaud, A. Korinek, T. Casagrande, R.C. Newman, G.A. Botton, Effects of boundary migration and pinning particles on intergranular oxidation revealed by 2D and 3D analytical electron microscopy, Acta Mater. 131 (2017) 280–295.
[43] L. Volpe, M.G. Burke, F. Scenini, Correlation between grain boundary migration and stress corrosion cracking of alloy 600 in hydrogenated steam, Acta Mater. 186 (2020) 454–466.
[44] L. Volpe, M.G. Burke, F. Scenini, Understanding the role of diffusion induced grain boundary migration on the preferential intergranular oxidation behaviour of alloy 600 via advanced microstructural characterization, Acta Mater. 175 (2019) 238–249.
[45] W. Kuang, G.S. Was, A high-resolution characterization of the initiation of stress corrosion crack in alloy 690 in simulated pressurized water reactor primary water, Corros. Sci. 163 (2020), 108243.
[46] W. Kuang, M. Song, G.S. Was, Insights into the stress corrosion cracking of solution annealed alloy 690 in simulated pressurized water reactor primary water under dynamic straining, Acta Mater. 151 (2018) 321–333.
[47] S.-P. Tsai, S.K. Makineni, B. Gault, K. Kawano-Miyata, A. Taniyama, S. Zaefferer, Precipitation formation on Σ5 and Σ7 grain boundaries in 316L stainless steel and their roles on intergranular corrosion, Acta Mater. 210 (2021), 116822.
[48] W. Kuang, M. Song, P. Wang, G.S. Was, The oxidation of alloy 690 in simulated pressurized water reactor primary water, Corros. Sci. 126 (2017) 227–237.
[49] Z. Wang, Investigation of Crystallographic Character and Molten-salt corrosion Properties of Grain Boundaries in a Stainless Steel Using EBSD and Ab-initio Calculations (Ph.D. thesis), Ruhr-Universität Bochum, 2017.
[50] S.Y. Persaud, A. Korinek, J. Huang, G.A. Botton, R.C. Newman, Internal oxidation of alloy 600 exposed to hydrogenated steam and the beneficial effects of thermal treatment, Corros. Sci. 86 (2014) 108–122.
[51] G. Bertali, F. Scenini, M.G. Burke, The effect of residual stress on the preferential intergranular oxidation of alloy 600, Corros. Sci. 111 (2016) 494–507.
[52] G. Bertali, M.G. Burke, F. Scenini, N. Huin, The effect of temperature on the preferential intergranular oxidation susceptibility of alloy 600, Metall. Mater. Trans. A 49 (2018) 1879–1894.
[53] Z. Shen, P. Karamched, K. Arioka, S. Lozano-Perez, Observation and quantification of the diffusion-induced grain boundary migration ahead of SCC crack tips, Corros. Sci. 147 (2019) 163–168.
[54] T. Fujii, K. Tohgo, Y. Mori, Y. Shimamura, Crystallography of intergranular corrosion in sensitized austenitic stainless steel, Mater. Charact. 144 (2018) 219–226.
[55] T. Fujii, T. Furumoto, K. Tohgo, Y. Shimamura, Crystallographic evaluation of susceptibility to intergranular corrosion in austenitic stainless steel with various degrees of sensitization, Materials 13 (2020) 613.
[56] H.Y. Lee, S.-J.L. Kang, D.Y. Yoon, The effect of elastic anisotropy on the direction and faceting of chemically induced grain boundary migration in Al_2O_3, Acta Metall. Mater. 41 (1993) 2497–2502.
[57] T. Hu, S. Yang, N. Zhou, Y. Zhang, J. Luo, Role of disordered bipolar complexions on the sulfur embrittlement of nickel general grain boundaries, Nat. Commun. 9 (2018) 2764.
[58] Z. Yu, P.R. Cantwell, Q. Gao, D. Yin, Y. Zhang, N. Zhou, G.S. Rohrer, M. Widom, J. Luo, M.P. Harmer, Segregation-induced ordered superstructures at general grain boundaries in a nickel bismuth alloy, Science 358 (6359) (2017) 97–101.
[59] J.P. Hanson, A. Bagri, J. Lind, P. Kenesei, R.M. Suter, S. Gradecak, M. J. Demkowicz, Crystallographic character of grain boundaries resistant to hydrogen-assisted fracture in Ni-base alloy 725, Nat. Commun. 9 (1) (2018) 3386.
[60] D. Wolf, K.L. Merkle, in: D. Wolf, S. Yip (Eds.), Materials Interfaces, Chapman and Hall, London, 1992, p. 87.
[61] H. Miyamoto, K. Ikeuchi, T. Mimaki, The role of grain boundary plane orientation on intergranular corrosion of symmetric and asymmetric [110] tilt grain boundaries in directionally solidified pure copper, Scr. Mater. 50 (2004) 1417–1421.
[62] J. Li, S.J. Dillon, G.S. Rohrer, Relative grain boundary area and energy distributions in nickel, Acta Mater. 57 (2009) 4304–4311.
[63] Y.T. Tang, P. Karamched, J. Liu, J.C. Haley, R.C. Reed, A.J. Wilkinson, Grain boundary serration in nickel alloy inconel 600: quantification and mechanisms, Acta Mater. 181 (2019) 352–366.
[64] H.U. Hong, I.S. Kim, B.G. Choi, M.Y. Kim, C.Y. Jo, The effect of grain boundary serration on creep resistance in a wrought nickel-based superalloy, Mater. Sci. Eng. A 517 (2009) 125–131.
[65] H.U. Hong, H.W. Jeong, I.S. Kim, B.G. Choi, Y.S. Yoo, C.Y. Jo, Significant decrease in interfacial energy of grain boundary through serrated grain boundary transition, Philos. Mag. 92 (2012) 2809–2825.
[66] K.J. Kim, H.U. Hong, S.W. Nam, Investigation on the formation of serrated grain boundaries with grain boundary characteristics in an AISI 316 stainless steel, J. Nucl. Mater. 393 (2009) 249–253.
[67] D. Wolf, A broken-bond model for grain boundaries in face-centered cubic metals, J. Appl. Phys. 68 (1990) 3221–3236.
[68] D. Wolf, Correlation between structure, energy, and ideal cleavage fracture for symmetrical grain boundaries in fcc metals, J. Mater. Res. 5 (1990) 1708–1730.
[69] V. Randle, G.S. Rohrer, H.M. Miller, M. Coleman, G.T. Owen, Five-parameter grain boundary distribution of commercially grain boundary engineered nickel and copper, Acta Mater. 56 (2008) 2363–2373.
[70] D. Wolf, S. Phillpot, Role of the densest lattice planes in the stability of crystalline interfaces: a computer simulation study, Mater. Sci. Eng. A 107 (1989) 3–14.
[71] A.P. Sutton, Irrational interfaces, Prog. Mater. Sci. 36 (1992) 167–202.